FERMILAB-PUB-11-190-E

Measurement of $\sin^2\theta^{\ell}_{\rm eff}$ and Z-light quark couplings using the forward-backward charge asymmetry in $p\bar{p} \to Z/\gamma^* \to e^+e^-$ events with $\mathcal{L} = 5.0$ fb^{-1} at $\sqrt{s} = 1.96$ TeV

V.M. Abazov,[35] B. Abbott,[73] B.S. Acharya,[29] M. Adams,[49] T. Adams,[47] G.D. Alexeev,[35] G. Alkhazov,[39] A. Alton[a],[61] G. Alverson,[60] G.A. Alves,[2] L.S. Ancu,[34] M. Aoki,[48] M. Arov,[58] A. Askew,[47] B. Åsman,[41] O. Atramentov,[65] C. Avila,[8] J. BackusMayes,[80] F. Badaud,[13] L. Bagby,[48] B. Baldin,[48] D.V. Bandurin,[47] S. Banerjee,[29] E. Barberis,[60] P. Baringer,[56] J. Barreto,[3] J.F. Bartlett,[48] U. Bassler,[18] V. Bazterra,[49] S. Beale,[6] A. Bean,[56] M. Begalli,[3] M. Begel,[71] C. Belanger-Champagne,[41] L. Bellantoni,[48] S.B. Beri,[27] G. Bernardi,[17] R. Bernhard,[22] I. Bertram,[42] M. Besançon,[18] R. Beuselinck,[43] V.A. Bezzubov,[38] P.C. Bhat,[48] V. Bhatnagar,[27] G. Blazey,[50] S. Blessing,[47] K. Bloom,[64] A. Boehnlein,[48] D. Boline,[70] E.E. Boos,[37] G. Borissov,[42] T. Bose,[59] A. Brandt,[76] O. Brandt,[23] R. Brock,[62] G. Brooijmans,[68] A. Bross,[48] D. Brown,[17] J. Brown,[17] X.B. Bu,[48] M. Buehler,[79] V. Buescher,[24] V. Bunichev,[37] S. Burdin[b],[42] T.H. Burnett,[80] C.P. Buszello,[41] B. Calpas,[15] E. Camacho-Pérez,[32] M.A. Carrasco-Lizarraga,[56] B.C.K. Casey,[48] H. Castilla-Valdez,[32] S. Chakrabarti,[70] D. Chakraborty,[50] K.M. Chan,[54] A. Chandra,[78] G. Chen,[56] S. Chevalier-Théry,[18] D.K. Cho,[75] S.W. Cho,[31] S. Choi,[31] B. Choudhary,[28] S. Cihangir,[48] D. Claes,[64] J. Clutter,[56] M. Cooke,[48] W.E. Cooper,[48] M. Corcoran,[78] F. Couderc,[18] M.-C. Cousinou,[15] A. Croc,[18] D. Cutts,[75] A. Das,[45] G. Davies,[43] K. De,[76] S.J. de Jong,[34] E. De La Cruz-Burelo,[32] F. Déliot,[18] M. Demarteau,[48] R. Demina,[69] D. Denisov,[48] S.P. Denisov,[38] S. Desai,[48] C. Deterre,[18] K. DeVaughan,[64] H.T. Diehl,[48] M. Diesburg,[48] A. Dominguez,[64] T. Dorland,[80] A. Dubey,[28] L.V. Dudko,[37] D. Duggan,[65] A. Duperrin,[15] S. Dutt,[27] A. Dyshkant,[50] M. Eads,[64] D. Edmunds,[62] J. Ellison,[46] V.D. Elvira,[48] Y. Enari,[17] H. Evans,[52] A. Evdokimov,[71] V.N. Evdokimov,[38] G. Facini,[60] T. Ferbel,[69] F. Fiedler,[24] F. Filthaut,[34] W. Fisher,[62] H.E. Fisk,[48] M. Fortner,[50] H. Fox,[42] S. Fuess,[48] A. Garcia-Bellido,[69] V. Gavrilov,[36] P. Gay,[13] W. Geng,[15,62] D. Gerbaudo,[66] C.E. Gerber,[49] Y. Gershtein,[65] G. Ginther,[48,69] G. Golovanov,[35] A. Goussiou,[80] P.D. Grannis,[70] S. Greder,[19] H. Greenlee,[48] Z.D. Greenwood,[58] E.M. Gregores,[4] G. Grenier,[20] Ph. Gris,[13] J.-F. Grivaz,[16] A. Grohsjean,[18] S. Grünendahl,[48] M.W. Grünewald,[30] T. Guillemin,[16] F. Guo,[70] G. Gutierrez,[48] P. Gutierrez,[73] A. Haas[c],[68] S. Hagopian,[47] J. Haley,[60] L. Han,[7] K. Harder,[44] A. Harel,[69] J.M. Hauptman,[55] J. Hays,[43] T. Head,[44] T. Hebbeker,[21] D. Hedin,[50] H. Hegab,[74] A.P. Heinson,[46] U. Heintz,[75] C. Hensel,[23] I. Heredia-De La Cruz,[32] K. Herner,[61] G. Hesketh[d],[44] M.D. Hildreth,[54] R. Hirosky,[79] T. Hoang,[47] J.D. Hobbs,[70] B. Hoeneisen,[12] M. Hohlfeld,[24] Z. Hubacek,[10,18] N. Huske,[17] V. Hynek,[10] I. Iashvili,[67] R. Illingworth,[48] A.S. Ito,[48] S. Jabeen,[75] M. Jaffré,[16] D. Jamin,[15] A. Jayasinghe,[73] R. Jesik,[43] K. Johns,[45] M. Johnson,[48] D. Johnston,[64] A. Jonckheere,[48] P. Jonsson,[43] J. Joshi,[27] A.W. Jung,[48] A. Juste,[40] K. Kaadze,[57] E. Kajfasz,[15] D. Karmanov,[37] P.A. Kasper,[48] I. Katsanos,[64] R. Kehoe,[77] S. Kermiche,[15] N. Khalatyan,[48] A. Khanov,[74] A. Kharchilava,[67] Y.N. Kharzheev,[35] D. Khatidze,[75] M.H. Kirby,[51] J.M. Kohli,[27] A.V. Kozelov,[38] J. Kraus,[62] S. Kulikov,[38] A. Kumar,[67] A. Kupco,[11] T. Kurča,[20] V.A. Kuzmin,[37] J. Kvita,[9] S. Lammers,[52] G. Landsberg,[75] P. Lebrun,[20] H.S. Lee,[31] S.W. Lee,[55] W.M. Lee,[48] J. Lellouch,[17] L. Li,[46] Q.Z. Li,[48] S.M. Lietti,[5] J.K. Lim,[31] D. Lincoln,[48] J. Linnemann,[62] V.V. Lipaev,[38] R. Lipton,[48] Y. Liu,[7] Z. Liu,[6] A. Lobodenko,[39] M. Lokajicek,[11] R. Lopes de Sa,[70] H.J. Lubatti,[80] R. Luna-Garcia[e],[32] A.L. Lyon,[48] A.K.A. Maciel,[2] D. Mackin,[78] R. Madar,[18] R. Magaña-Villalba,[32] S. Malik,[64] V.L. Malyshev,[35] Y. Maravin,[57] J. Martínez-Ortega,[32] R. McCarthy,[70] C.L. McGivern,[56] M.M. Meijer,[34] A. Melnitchouk,[63] D. Menezes,[50] P.G. Mercadante,[4] M. Merkin,[37] A. Meyer,[21] J. Meyer,[23] F. Miconi,[19] N.K. Mondal,[29] G.S. Muanza,[15] M. Mulhearn,[79] E. Nagy,[15] M. Naimuddin,[28] M. Narain,[75] R. Nayyar,[28] H.A. Neal,[61] J.P. Negret,[8] P. Neustroev,[39] S.F. Novaes,[5] T. Nunnemann,[25] G. Obrant,[39] J. Orduna,[78] N. Osman,[15] J. Osta,[54] G.J. Otero y Garzón,[1] M. Padilla,[46] A. Pal,[76] N. Parashar,[53] V. Parihar,[75] S.K. Park,[31] J. Parsons,[68] R. Partridge[c],[75] N. Parua,[52] A. Patwa,[71] B. Penning,[48] M. Perfilov,[37] K. Peters,[44] Y. Peters,[44] K. Petridis,[44] G. Petrillo,[69] P. Pétroff,[16] R. Piegaia,[1] J. Piper,[62] M.-A. Pleier,[71] P.L.M. Podesta-Lerma[f],[32] V.M. Podstavkov,[48] P. Polozov,[36] A.V. Popov,[38] M. Prewitt,[78] D. Price,[52] N. Prokopenko,[38] S. Protopopescu,[71] J. Qian,[61] A. Quadt,[23] B. Quinn,[63] M.S. Rangel,[2] K. Ranjan,[28] P.N. Ratoff,[42] I. Razumov,[38] P. Renkel,[77] M. Rijssenbeek,[70] I. Ripp-Baudot,[19] F. Rizatdinova,[74] M. Rominsky,[48] A. Ross,[42] C. Royon,[18] P. Rubinov,[48] R. Ruchti,[54] G. Safronov,[36] G. Sajot,[14] P. Salcido,[50] A. Sánchez-Hernández,[32] M.P. Sanders,[25] B. Sanghi,[48] A.S. Santos,[5] G. Savage,[48] L. Sawyer,[58] T. Scanlon,[43] R.D. Schamberger,[70] Y. Scheglov,[39] H. Schellman,[51] T. Schliephake,[26] S. Schlobohm,[80] C. Schwanenberger,[44]

R. Schwienhorst,[62] J. Sekaric,[56] H. Severini,[73] E. Shabalina,[23] V. Shary,[18] A.A. Shchukin,[38] R.K. Shivpuri,[28] V. Simak,[10] V. Sirotenko,[48] P. Skubic,[73] P. Slattery,[69] D. Smirnov,[54] K.J. Smith,[67] G.R. Snow,[64] J. Snow,[72] S. Snyder,[71] S. Söldner-Rembold,[44] L. Sonnenschein,[21] K. Soustruznik,[9] J. Stark,[14] V. Stolin,[36] D.A. Stoyanova,[38] M. Strauss,[73] D. Strom,[49] L. Stutte,[48] L. Suter,[44] P. Svoisky,[73] M. Takahashi,[44] A. Tanasijczuk,[1] W. Taylor,[6] M. Titov,[18] V.V. Tokmenin,[35] Y.-T. Tsai,[69] D. Tsybychev,[70] B. Tuchming,[18] C. Tully,[66] L. Uvarov,[39] S. Uvarov,[39] S. Uzunyan,[50] R. Van Kooten,[52] W.M. van Leeuwen,[33] N. Varelas,[49] E.W. Varnes,[45] I.A. Vasilyev,[38] P. Verdier,[20] L.S. Vertogradov,[35] M. Verzocchi,[48] M. Vesterinen,[44] D. Vilanova,[18] P. Vokac,[10] H.D. Wahl,[47] M.H.L.S. Wang,[69] J. Warchol,[54] G. Watts,[80] M. Wayne,[54] M. Weber[g],[48] L. Welty-Rieger,[51] A. White,[76] D. Wicke,[26] M.R.J. Williams,[42] G.W. Wilson,[56] M. Wobisch,[58] D.R. Wood,[60] T.R. Wyatt,[44] Y. Xie,[48] C. Xu,[61] S. Yacoob,[51] R. Yamada,[48] W.-C. Yang,[44] T. Yasuda,[48] Y.A. Yatsunenko,[35] Z. Ye,[48] H. Yin,[48] K. Yip,[71] S.W. Youn,[48] J. Yu,[76] S. Zelitch,[79] T. Zhao,[80] B. Zhou,[61] J. Zhu,[61] M. Zielinski,[69] D. Zieminska,[52] and L. Zivkovic[75]

(The D0 Collaboration*)

[1] *Universidad de Buenos Aires, Buenos Aires, Argentina*
[2] *LAFEX, Centro Brasileiro de Pesquisas Físicas, Rio de Janeiro, Brazil*
[3] *Universidade do Estado do Rio de Janeiro, Rio de Janeiro, Brazil*
[4] *Universidade Federal do ABC, Santo André, Brazil*
[5] *Instituto de Física Teórica, Universidade Estadual Paulista, São Paulo, Brazil*
[6] *Simon Fraser University, Vancouver, British Columbia, and York University, Toronto, Ontario, Canada*
[7] *University of Science and Technology of China, Hefei, People's Republic of China*
[8] *Universidad de los Andes, Bogotá, Colombia*
[9] *Charles University, Faculty of Mathematics and Physics, Center for Particle Physics, Prague, Czech Republic*
[10] *Czech Technical University in Prague, Prague, Czech Republic*
[11] *Center for Particle Physics, Institute of Physics, Academy of Sciences of the Czech Republic, Prague, Czech Republic*
[12] *Universidad San Francisco de Quito, Quito, Ecuador*
[13] *LPC, Université Blaise Pascal, CNRS/IN2P3, Clermont, France*
[14] *LPSC, Université Joseph Fourier Grenoble 1, CNRS/IN2P3, Institut National Polytechnique de Grenoble, Grenoble, France*
[15] *CPPM, Aix-Marseille Université, CNRS/IN2P3, Marseille, France*
[16] *LAL, Université Paris-Sud, CNRS/IN2P3, Orsay, France*
[17] *LPNHE, Universités Paris VI and VII, CNRS/IN2P3, Paris, France*
[18] *CEA, Irfu, SPP, Saclay, France*
[19] *IPHC, Université de Strasbourg, CNRS/IN2P3, Strasbourg, France*
[20] *IPNL, Université Lyon 1, CNRS/IN2P3, Villeurbanne, France and Université de Lyon, Lyon, France*
[21] *III. Physikalisches Institut A, RWTH Aachen University, Aachen, Germany*
[22] *Physikalisches Institut, Universität Freiburg, Freiburg, Germany*
[23] *II. Physikalisches Institut, Georg-August-Universität Göttingen, Göttingen, Germany*
[24] *Institut für Physik, Universität Mainz, Mainz, Germany*
[25] *Ludwig-Maximilians-Universität München, München, Germany*
[26] *Fachbereich Physik, Bergische Universität Wuppertal, Wuppertal, Germany*
[27] *Panjab University, Chandigarh, India*
[28] *Delhi University, Delhi, India*
[29] *Tata Institute of Fundamental Research, Mumbai, India*
[30] *University College Dublin, Dublin, Ireland*
[31] *Korea Detector Laboratory, Korea University, Seoul, Korea*
[32] *CINVESTAV, Mexico City, Mexico*
[33] *FOM-Institute NIKHEF and University of Amsterdam/NIKHEF, Amsterdam, The Netherlands*
[34] *Radboud University Nijmegen/NIKHEF, Nijmegen, The Netherlands*
[35] *Joint Institute for Nuclear Research, Dubna, Russia*
[36] *Institute for Theoretical and Experimental Physics, Moscow, Russia*
[37] *Moscow State University, Moscow, Russia*
[38] *Institute for High Energy Physics, Protvino, Russia*
[39] *Petersburg Nuclear Physics Institute, St. Petersburg, Russia*
[40] *Institució Catalana de Recerca i Estudis Avançats (ICREA) and Institut de Física d'Altes Energies (IFAE), Barcelona, Spain*
[41] *Stockholm University, Stockholm and Uppsala University, Uppsala, Sweden*
[42] *Lancaster University, Lancaster LA1 4YB, United Kingdom*
[43] *Imperial College London, London SW7 2AZ, United Kingdom*
[44] *The University of Manchester, Manchester M13 9PL, United Kingdom*
[45] *University of Arizona, Tucson, Arizona 85721, USA*

[46] University of California Riverside, Riverside, California 92521, USA
[47] Florida State University, Tallahassee, Florida 32306, USA
[48] Fermi National Accelerator Laboratory, Batavia, Illinois 60510, USA
[49] University of Illinois at Chicago, Chicago, Illinois 60607, USA
[50] Northern Illinois University, DeKalb, Illinois 60115, USA
[51] Northwestern University, Evanston, Illinois 60208, USA
[52] Indiana University, Bloomington, Indiana 47405, USA
[53] Purdue University Calumet, Hammond, Indiana 46323, USA
[54] University of Notre Dame, Notre Dame, Indiana 46556, USA
[55] Iowa State University, Ames, Iowa 50011, USA
[56] University of Kansas, Lawrence, Kansas 66045, USA
[57] Kansas State University, Manhattan, Kansas 66506, USA
[58] Louisiana Tech University, Ruston, Louisiana 71272, USA
[59] Boston University, Boston, Massachusetts 02215, USA
[60] Northeastern University, Boston, Massachusetts 02115, USA
[61] University of Michigan, Ann Arbor, Michigan 48109, USA
[62] Michigan State University, East Lansing, Michigan 48824, USA
[63] University of Mississippi, University, Mississippi 38677, USA
[64] University of Nebraska, Lincoln, Nebraska 68588, USA
[65] Rutgers University, Piscataway, New Jersey 08855, USA
[66] Princeton University, Princeton, New Jersey 08544, USA
[67] State University of New York, Buffalo, New York 14260, USA
[68] Columbia University, New York, New York 10027, USA
[69] University of Rochester, Rochester, New York 14627, USA
[70] State University of New York, Stony Brook, New York 11794, USA
[71] Brookhaven National Laboratory, Upton, New York 11973, USA
[72] Langston University, Langston, Oklahoma 73050, USA
[73] University of Oklahoma, Norman, Oklahoma 73019, USA
[74] Oklahoma State University, Stillwater, Oklahoma 74078, USA
[75] Brown University, Providence, Rhode Island 02912, USA
[76] University of Texas, Arlington, Texas 76019, USA
[77] Southern Methodist University, Dallas, Texas 75275, USA
[78] Rice University, Houston, Texas 77005, USA
[79] University of Virginia, Charlottesville, Virginia 22901, USA
[80] University of Washington, Seattle, Washington 98195, USA

(Dated: June 28, 2011)

We measure the mass dependence of the forward-backward charge asymmetry in 157,553 $p\bar{p} \to Z/\gamma^* \to e^+e^-$ interactions, corresponding to 5.0 fb^{-1} of integrated luminosity collected by the D0 experiment at the Fermilab Tevatron Collider at $\sqrt{s} = 1.96$ TeV. The effective weak mixing angle ($\theta^\ell_{\rm eff}$) from this process involving predominantly the first generation of quarks is extracted as $\sin^2\theta^\ell_{\rm eff} = 0.2309 \pm 0.0008$ (stat.) $\pm$ 0.0006 (syst.). We also present the most precise direct measurement of the vector and axial-vector couplings of u and d quarks to the Z boson.

PACS numbers: 12.15.Ji, 12.15.Mn, 13.85.Qk, 14.70.Hp, 13.38.Dg

INTRODUCTION

Electron-positron pairs (e^+e^-) can be produced through the Drell-Yan process over a large invariant mass range at the Fermilab Tevatron Collider. In the standard model (SM) of particle physics, the process occurs to first order via $q\bar{q}$ annihilation into a real (or virtual) Z boson or a virtual photon (γ^*). While the coupling of a fermion (f) to the photon is purely a vector coupling, the coupling of the same fermion to the Z boson has both vector (g_V^f) and axial-vector (g_A^f) components:

$$\begin{aligned} g_V^f &= I_3^f - 2q_f \cdot \sin^2\theta_W, \\ g_A^f &= I_3^f, \end{aligned} \tag{1}$$

where I_3^f and q_f are the third component of the weak isospin and the charge of the fermion, and θ_W is the weak mixing angle [1]. The presence of both vector and axial-vector couplings gives rise to an asymmetry in the distribution of the polar angle θ^* of the negatively charged lepton relative to the incoming quark direction in the rest frame of the lepton pair. To minimize the effect of the unknown transverse momentum of the incoming quarks,

*with visitors from [a]Augustana College, Sioux Falls, SD, USA, [b]The University of Liverpool, Liverpool, UK, [c]SLAC, Menlo Park, CA, USA, [d]University College London, London, UK, [e]Centro de Investigacion en Computacion - IPN, Mexico City, Mexico, [f]ECFM, Universidad Autonoma de Sinaloa, Culiacán, Mexico, and [g]Universität Bern, Bern, Switzerland.

we calculate θ^* in the Collins-Soper reference frame [2] as

$$\cos\theta^* = \frac{2}{|Q|\sqrt{Q^2+Q_T^2}}(P_l^+ P_{\bar{l}}^- - P_l^- P_{\bar{l}}^+), \qquad (2)$$

where Q (Q_T) is the four momentum (transverse momentum) of the lepton pair, and P_l and $P_{\bar{l}}$ are the four momenta of the lepton and anti-lepton, respectively. They are measured in the lab frame, and the momenta $P_l^\pm$ are defined as

$$P_l^\pm = \frac{1}{\sqrt{2}}(P_l^0 \pm P_l^3), \qquad (3)$$

where P_l^0 and P_l^3 are the energy and the longitudinal component of the lepton momentum, respectively. In the Collins-Soper frame, the polar axis is defined as the bisector of the proton beam momentum $\boldsymbol{P_1}$ and the negative of the anti-proton beam momentum, $-\boldsymbol{P_2}$, when the proton and anti-proton are boosted into the rest frame of the lepton pair, as shown in Fig. 1 [3].

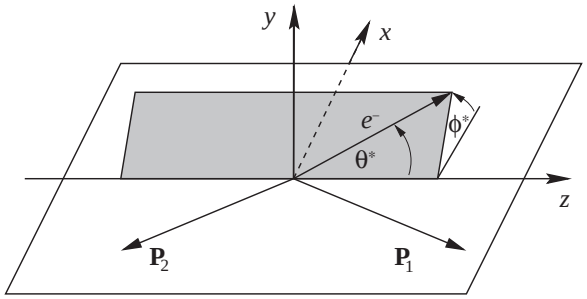

FIG. 1: The Collins-Soper reference frame. The bisector of the proton beam momentum $\boldsymbol{P_1}$ and the negative of the anti-proton beam momentum $-\boldsymbol{P_2}$ are used to measure the angle θ^*. The momenta $\boldsymbol{P_1}$ and $\boldsymbol{P_2}$ are measured in the e^+e^- rest frame.

Events with electron $\cos\theta^* > 0$ are classified as forward (F), and those with electron $\cos\theta^* < 0$ are classified as backward (B). The forward-backward charge asymmetry, A_{FB}, is defined by

$$A_{FB} = \frac{\sigma_F - \sigma_B}{\sigma_F + \sigma_B}, \qquad (4)$$

where σ_F and σ_B are the cross sections for forward and backward processes, respectively.

The SM leading order (LO) prediction [4] for A_{FB} as a function of the dielectron invariant mass (M_{ee}) is shown in Fig. 2 for $u\bar{u} \to Z/\gamma^* \to e^+e^-$, $d\bar{d} \to Z/\gamma^* \to e^+e^-$, and $p\bar{p} \to Z/\gamma^* \to e^+e^-$ with the CTEQ6L1 parton distribution functions (PDFs) [5]. Around the Z pole, the asymmetry is proportional to both the vector and axial-vector couplings of the Z boson to the fermions and is numerically close to 0. At large invariant mass, the asymmetry is dominated by Z/γ^* interference and is almost constant (≈ 0.6). In the high mass region, the A_{FB} measurement can be used to investigate possible new phenomena that may alter A_{FB}, such as new neutral gauge bosons or large extra dimensions [6–14].

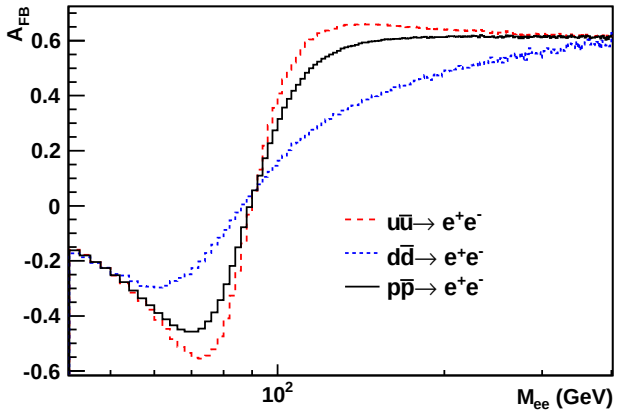

FIG. 2: [color online] The SM LO A_{FB} prediction as a function of the dielectron invariant mass for $u\bar{u} \to e^+e^-$, $d\bar{d} \to e^+e^-$, and $p\bar{p} \to e^+e^-$ [4].

In the vicinity of the Z pole, A_{FB} is sensitive to the effective weak mixing angle ($\sin^2\theta^f_{\rm eff}$) for each fermion species, f, involved in a particular measurement. To all orders in perturbation theory [1, 15], $\sin^2\theta^f_{\rm eff}$ is related to the vector and axial-vector couplings by the expression

$$g_V^f/g_A^f = 1 - 4|q_f|\sin^2\theta^f_{\rm eff}. \qquad (5)$$

This charged lepton effective mixing angle $\sin^2\theta^\ell_{\rm eff}$ varies as a function of the momentum transfer at which it is measured. Conventionally, it is quoted at the Z pole $\left[\sin^2\theta^\ell_{\rm eff}(M_Z)\right]$, and it is identical for e, μ, and τ leptons, due to lepton universality.

In the SM, asymmetries measured at the Z pole [15] depend only on the value of $\sin^2\theta^f_{\rm eff}$ for the fermions being considered. Because of the small ratio of vector and axial-vector couplings for leptons, the sensitivity of leptonic asymmetries to the changes in effective mixing angle arises predominantly through the variation of the leptonic couplings and not those of the quarks. Therefore, it is customary to express A_{FB} measurements in terms of $\sin^2\theta^\ell_{\rm eff}$. In order to extract $\sin^2\theta^\ell_{\rm eff}$ from A_{FB} under a consistent SM definition and compare results with previous measurements, we take into account the difference between the electroweak radiative corrections for electrons and u/d quarks using the relations [15–17]

$$\begin{aligned}\sin^2\theta^u_{\rm eff} &= \sin^2\theta^\ell_{\rm eff} - 0.0001,\\ \sin^2\theta^d_{\rm eff} &= \sin^2\theta^\ell_{\rm eff} - 0.0002.\end{aligned} \qquad (6)$$

Precise determinations of $\sin^2\theta^\ell_{\rm eff}$ have been made in many processes at different Q^2 scales. They include atomic parity violation ($|Q^2| \approx 10^{-18}$ GeV^2) [18], Møller

scattering using a polarized electron beam and unpolarized target ($|Q^2| \approx 0.03$ GeV^2) [19], the NuTeV deep inelastic neutrino and anti-neutrino scattering on iron ($|Q^2| \approx 4$ GeV^2) [20], and a number of measurements employing e^+e^- collisions by the LEP and SLD Collaborations ($|Q^2| \approx M_Z^2$) [15]. The current world average value of $\sin^2\theta^\ell_{\rm eff}$ is 0.23153±0.00016 [15]. The two most precise determinations of $\sin^2\theta^\ell_{\rm eff}$ come from the b-quark forward-backward asymmetry at LEP, $A_{FB}^{0,b}$, with $\sin^2\theta^\ell_{\rm eff} = 0.23221 \pm 0.00029$, and the left-right asymmetry at SLD, A_{lr}(SLD), with $\sin^2\theta^\ell_{\rm eff} = 0.23098 \pm 0.00026$. These two measurements differ from each other by about three standard deviations, and deviate by +2.1 standard deviations and −1.8 standard deviations from the global fit, respectively.

The LEP Collaborations also measured $\sin^2\theta^\ell_{\rm eff}$ from the inclusive hadronic charge asymmetry ($Q_{FB}^{\rm had}$), with larger uncertainties governed by the ambiguity of charge separation for final state quark species. Furthermore, the hadronic charge asymmetry arising from u- and d-type quarks are in opposite directions, partially canceling. Thus, modifications to the SM that would affect only u and d quark couplings are poorly constrained. Drell-Yan processes at hadron colliders, in which the initial state is dominated by the light u and d quarks in the proton, provide a much less ambiguous measurement of the light quark couplings. The dominant systematic uncertainty at the Tevatron originates from the quark composition of the proton and anti-proton, which has been well constrained and parametrized by PDFs [5]. The use of the Collins-Soper frame reduces possible confounding effects from higher order quantum chromodynamics (QCD) corrections.

Previous direct measurements of u and d quark couplings to the Z boson are of limited precision ([15, 21, 22]). With precise determination of the leptonic couplings from LEP and SLD, we can interpret the measurement of the forward-backward asymmetry directly in terms of the vector and axial-vector couplings of the u/d quarks.

At the Tevatron, measurements of the A_{FB}, $\sin^2\theta^\ell_{\rm eff}$, $g_V^{u(d)}$ and $g_A^{u(d)}$ have been performed by the CDF and D0 Collaborations [21, 23–25]. The largest integrated luminosity used for these measurements was 1.1 fb^{-1} for A_{FB} and $\sin^2\theta^\ell_{\rm eff}$ measurements [25], and 72 pb^{-1} for $g_V^{u(d)}$ and $g_A^{u(d)}$ measurements [21]. In this Article we present new measurements of the quantities $\sin^2\theta^\ell_{\rm eff}$, $g_V^{u(d)}$ and $g_A^{u(d)}$ based on 5.0 fb^{-1} of integrated luminosity [26], collected using the D0 detector [27] between April 2002 and April 2009.

APPARATUS AND EVENT SELECTION

The D0 detector [27] comprises a central tracking system, a calorimeter and a muon system. The central tracking system is composed of a silicon microstrip tracker (SMT) and a central fiber tracker (CFT), both located within a 2 T superconducting solenoidal magnet and optimized for tracking and vertexing capabilities at detector pseudorapidities of $|\eta_{\rm det}| < 3$ [28]. Three liquid argon and uranium calorimeters provide coverage of $|\eta_{\rm det}| < 3.2$ for electrons with gaps between cryostats creating an inefficient electron detection region between $1.0 < |\eta_{\rm det}| < 1.5$. The electromagnetic (EM) section of the calorimeter is segmented into four longitudinal layers with transverse segmentation of $\Delta\eta \times \Delta\phi = 0.1 \times 0.1$, except for the third layer, where it is 0.05×0.05. The calorimeter is well suited for a precise measurement of electron and photon energies, providing a resolution of $\approx 3.6\%$ at an incident energy of ≈ 50 GeV. The muon system surrounds the calorimetry and consists of three layers of scintillators and drift tubes and 1.8 T iron toroids with a coverage of $|\eta_{\rm det}| < 2$. The three-level trigger system and data acquisition systems are designed to accommodate the high instantaneous luminosity of Run II. A logical OR of dielectron triggers is used to collect the data, resulting in a trigger efficiency close to 100% for signal events that passed the offline selection.

To select $Z/\gamma^* \to e^+e^-$ events, we require two EM shower candidates with transverse energy $E_T > 25$ GeV measured in the calorimeter. An isolation cut is imposed on the candidates, requiring that the fraction of their energy in an annular central (endcap) calorimeter cone of radius $0.2 < \Delta\mathcal{R} < 0.4$ must be less than 15% (10%) of the energy in the cone of $\Delta\mathcal{R} < 0.2$, where $\Delta\mathcal{R} = \sqrt{(\Delta\eta)^2 + (\Delta\phi)^2}$. The candidates are further required to have a significant fraction of their energy deposited in the EM calorimeter compared to that in the hadron calorimeter, and to have a shower shape consistent with that expected for an electron. At least one electron candidate is required to be in the central ($|\eta_{\rm det}| < 1.0$) fiducial region and spatially matched to a reconstructed track, while the other candidate may be either in the central or endcap ($1.5 < |\eta_{\rm det}| < 2.5$) calorimeter. No track requirement is imposed on candidates in the endcap calorimeter, since the track reconstruction efficiency is degraded in this region. If an event has both candidates in the central calorimeter (CC events), the two candidates are further required to have opposite charges. For events with one candidate in the central and the other in the endcap calorimeter (CE events), the charge of the central EM candidate is used to determine if it is a forward or a backward event. To suppress multijet background in CE events, the electron candidates in the endcap calorimeter are required to pass isolation criteria in the tracker, requiring the scalar sum

of the transverse momenta of tracks in the annulus $0.05 < \Delta\mathcal{R} < 0.4$ centered around the electron direction to be smaller than 1.5 GeV. Events are further required to have the reconstructed $p\bar{p}$ interaction vertex within 40 cm of the detector center in the coordinate along the z axis and a reconstructed invariant mass of the electron pair (M_{ee}) between 50 and 1000 GeV.

A total of 157,553 events remain after application of all selection criteria, with 73,755 CC events and 83,798 CE events. The forward-backward charge asymmetries are measured in 15 M_{ee} bins in the range $50 < M_{ee} < 1000$ GeV. The bin widths are chosen considering the statistics of the sample and the mass resolution of the detector. The bin widths and the numbers of forward and backward events for each mass bin are listed in Table I.

SIGNAL AND BACKGROUNDS

Monte Carlo (MC) samples for the $Z/\gamma^* \to e^+e^-$ process are generated using the PYTHIA event generator with CTEQ6L1 PDFs, followed by a detailed GEANT-based simulation [29] of the D0 detector response. This simulation is then improved by corrections for observed deficiencies in the detector simulation and for higher order physical effects not included in PYTHIA.

The event selection criteria can result in different efficiencies for forward and backward events. The electron selection efficiencies are independently measured from $Z/\gamma^* \to e^+e^-$ events in data and in the MC, where one electron is selected in the central calorimeter using tight calorimeter shower shape cuts and track quality cuts, and the second electron is used as a probe to determine the detection efficiencies. These efficiencies are measured for forward and backward events separately. For data, the background in each mass bin is estimated and subtracted prior to the measurement of the efficiencies. The ratios between data and MC electron selection efficiencies for forward and backward candidates as a function of M_{ee} for electrons in the central calorimeter are shown in Fig. 3. The ratios are constant within statistical uncertainties, with the largest deviations observed in a few mass bins around 70 and 130 GeV. Efficiency corrections derived using data presented on Fig. 3 are applied to the MC separately for forward and backward events to account for the mis-modeling of electrons' shower shapes and track matching efficiencies. In addition, the MC is adjusted to reproduce the calorimeter energy scale and resolution, as well as the distributions of the instantaneous luminosity and the event vertex position observed in data.

Next-to-next-to-leading order (NNLO) QCD corrections [30] for Z/γ^* boson production are applied to the simulated PYTHIA sample by reweighting the M_{ee} distribution, and non-perturbative and next-to-leading order (NLO) corrections by reweighting the Z/γ^* boson transverse momentum and rapidity distributions [17, 31].

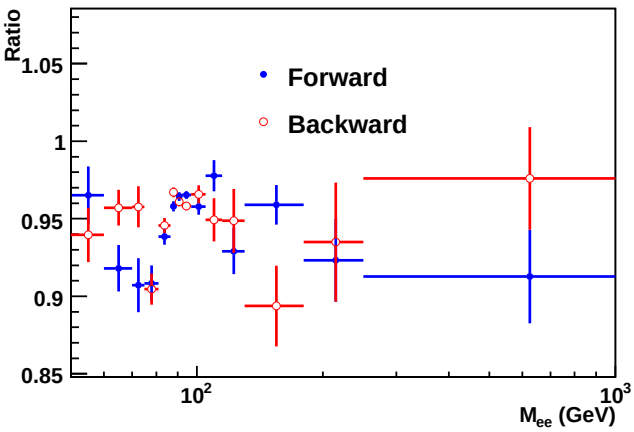

FIG. 3: [color online] The data/MC ratio of electron selection efficiencies as a function of invariant mass, for forward and backward events.

The effective mixing angle must be corrected to include higher order quantum electrodynamics (QED) and weak interaction contributions that are not present in our MC. These higher order corrections are determined using the ZGRAD2 program [16].

The largest background originates from multijet events in which jets are mis-reconstructed as electrons. Smaller background contributions arise from other SM processes that produce at least one real electron or photon in the final state. SM backgrounds, such as $Z/\gamma^* \to \tau\tau$, $W + X$, WW, WZ, $\gamma\gamma$, and $t\bar{t}$, are estimated using the MC. Higher order corrections to the cross sections have been applied [31–33]. The multijet background is estimated using collider data by fitting the M_{ee} distribution in the Z pole region (with other SM backgrounds subtracted) to the sum of the shape predicted by the corrected $Z/\gamma^* \to e^+e^-$ signal MC and the shape measured from a multijet-enriched sample. The multijet-enriched sample is selected by reversing the shower shape requirement on the two electron candidates. The average multijet background fraction over the entire mass region is found to be approximately 0.9%. The numbers of background events from each source in forward and backward samples are listed in Tables II and III.

Comparisons of data and the sum of signal and background for M_{ee} and $\cos\theta^*$ are shown in Figs. 4 and 5. In the M_{ee} bin 450–500 GeV, the data differ from the SM prediction by 1.8 standard deviations. Reasonable agreement is observed for all distributions in both forward and backward samples for all 15 M_{ee} bins. The CC and CE raw A_{FB} (not yet unfolded) distributions as functions of M_{ee} are then calculated from background-subtracted data.

TABLE I: Numbers of forward and backward CC and CE events in each M_{ee} bin after all selections.

M_{ee} (GeV)	CC		CE	
	Forward	Backward	Forward	Backward
$50-60$	276	319	54	70
$60-70$	464	711	238	413
$70-75$	411	545	285	495
$75-81$	852	1062	778	1240
$81-86.5$	3359	3559	3804	4245
$86.5-89.5$	6681	6642	8339	7591
$89.5-92$	9297	8717	11098	9534
$92-97$	12076	11109	14281	11412
$97-105$	2890	2173	3711	2150
$105-115$	680	431	1125	395
$115-130$	408	189	764	229
$130-180$	439	150	845	269
$180-250$	138	61	229	73
$250-500$	63	45	86	24
$500-1000$	7	1	1	0

TABLE II: Estimated number of background events in each M_{ee} bin in the forward sample.

M_{ee} (GeV)	$Z/\gamma^* \to \tau\tau$	$W+X$	WW	WZ	$\gamma\gamma$	$t\bar{t}$	Multijet
$50-60$	12.5 ± 0.91	11.7 ± 4.41	1.65 ± 0.14	0.14 ± 0.01	1.02 ± 0.35	1.00 ± 0.11	38.6 ± 0.04
$60-70$	29.4 ± 1.44	20.4 ± 7.17	3.29 ± 0.24	0.22 ± 0.01	3.10 ± 0.43	1.83 ± 0.21	$105. \pm 0.10$
$70-75$	16.6 ± 0.97	17.2 ± 4.38	1.68 ± 0.14	0.18 ± 0.01	1.08 ± 0.26	1.09 ± 0.13	69.2 ± 0.09
$75-81$	14.5 ± 0.91	16.6 ± 4.86	1.55 ± 0.13	0.31 ± 0.01	1.59 ± 0.28	1.37 ± 0.15	85.8 ± 0.10
$81-86.5$	5.16 ± 0.72	21.4 ± 8.33	1.82 ± 0.14	0.80 ± 0.03	2.26 ± 0.31	1.16 ± 0.14	80.3 ± 0.10
$86.5-89.5$	0.94 ± 0.49	8.03 ± 2.67	1.10 ± 0.12	1.72 ± 0.06	1.16 ± 0.26	0.56 ± 0.07	40.6 ± 0.07
$89.5-92$	1.63 ± 0.69	9.73 ± 3.07	0.86 ± 0.11	2.79 ± 0.11	0.29 ± 0.24	0.68 ± 0.08	31.0 ± 0.07
$92-97$	1.04 ± 0.49	18.9 ± 5.34	1.64 ± 0.14	3.66 ± 0.13	2.00 ± 0.30	0.99 ± 0.12	62.7 ± 0.10
$97-105$	1.38 ± 0.14	24.4 ± 10.8	2.72 ± 0.17	0.80 ± 0.03	2.00 ± 0.31	1.50 ± 0.15	88.5 ± 0.12
$105-115$	1.21 ± 0.11	23.4 ± 11.3	3.03 ± 0.19	0.33 ± 0.01	1.91 ± 0.30	1.22 ± 0.12	94.5 ± 0.12
$115-130$	1.33 ± 0.11	30.0 ± 15.5	4.33 ± 0.25	0.38 ± 0.01	2.00 ± 0.29	2.16 ± 0.19	$108. \pm 0.13$
$130-180$	2.38 ± 0.50	41.3 ± 27.6	9.87 ± 0.55	0.82 ± 0.03	4.51 ± 0.27	3.94 ± 0.40	$174. \pm 0.17$
$180-250$	0.57 ± 0.03	17.1 ± 14.5	4.53 ± 0.26	0.48 ± 0.02	2.84 ± 0.18	1.73 ± 0.17	42.5 ± 0.08
$250-500$	0.19 ± 0.02	4.80 ± 3.39	1.93 ± 0.15	0.25 ± 0.01	1.24 ± 0.12	0.53 ± 0.06	8.70 ± 0.04
$500-1000$	< 0.01	< 0.01	0.07 ± 0.00	< 0.01	0.04 ± 0.03	< 0.01	0.02 ± 0.00

TABLE III: Estimated number of background events in each M_{ee} bin in the backward sample.

M_{ee} (GeV)	$Z/\gamma^* \to \tau\tau$	$W+X$	WW	WZ	$\gamma\gamma$	$t\bar{t}$	Multijet
$50-60$	7.52 ± 0.80	4.27 ± 1.83	2.90 ± 0.20	0.20 ± 0.01	0.54 ± 0.25	1.40 ± 0.16	38.8 ± 0.04
$60-70$	26.2 ± 1.36	4.20 ± 2.39	3.73 ± 0.24	0.28 ± 0.01	2.85 ± 0.35	2.06 ± 0.24	$108. \pm 0.10$
$70-75$	12.4 ± 0.85	3.06 ± 1.33	2.64 ± 0.18	0.18 ± 0.01	2.32 ± 0.32	1.12 ± 0.12	70.2 ± 0.09
$75-81$	5.13 ± 0.72	2.74 ± 1.30	2.66 ± 0.18	0.34 ± 0.01	1.66 ± 0.28	1.21 ± 0.14	85.9 ± 0.10
$81-86.5$	1.10 ± 0.50	5.30 ± 2.49	1.68 ± 0.13	0.76 ± 0.03	2.33 ± 0.32	1.08 ± 0.13	78.8 ± 0.11
$86.5-89.5$	0.53 ± 0.49	4.25 ± 1.56	1.66 ± 0.14	1.59 ± 0.06	1.44 ± 0.27	0.45 ± 0.07	39.5 ± 0.08
$89.5-92$	0.15 ± 0.09	3.80 ± 1.67	1.32 ± 0.13	2.43 ± 0.09	1.09 ± 0.26	0.53 ± 0.07	31.5 ± 0.07
$92-97$	0.24 ± 0.10	2.34 ± 0.94	2.04 ± 0.14	3.17 ± 0.11	2.68 ± 0.34	1.05 ± 0.12	64.1 ± 0.10
$97-105$	0.30 ± 0.03	6.98 ± 2.64	3.93 ± 0.24	0.75 ± 0.02	2.20 ± 0.31	1.74 ± 0.20	90.0 ± 0.12
$105-115$	0.26 ± 0.03	5.47 ± 2.63	3.07 ± 0.19	0.35 ± 0.01	2.72 ± 0.34	1.53 ± 0.15	97.3 ± 0.12
$115-130$	0.46 ± 0.10	6.22 ± 3.89	3.25 ± 0.20	0.37 ± 0.01	2.60 ± 0.33	2.30 ± 0.24	$110. \pm 0.13$
$130-180$	0.76 ± 0.49	17.0 ± 10.2	5.58 ± 0.29	0.63 ± 0.03	4.97 ± 0.39	4.08 ± 0.40	$170. \pm 0.17$
$180-250$	0.30 ± 0.48	3.49 ± 2.92	2.42 ± 0.16	0.28 ± 0.01	3.01 ± 0.18	1.70 ± 0.17	46.3 ± 0.08
$250-500$	0.04 ± 0.01	0.62 ± 0.85	0.58 ± 0.11	0.08 ± 0.00	1.28 ± 0.20	0.50 ± 0.06	8.90 ± 0.04
$500-1000$	< 0.01	< 0.01	< 0.01	< 0.01	0.03 ± 0.00	< 0.01	0.02 ± 0.00

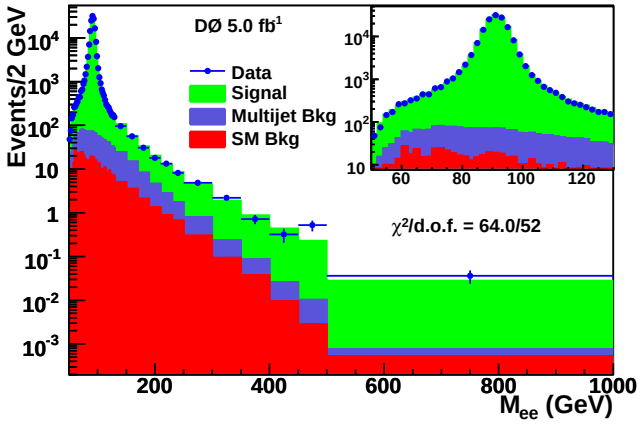

FIG. 4: [color online] Comparisons of the dielectron invariant mass between data and the sum of signal and background predictions for combined CC and CE events. The insert focuses on the Z pole region from 50 GeV to 130 GeV, where good agreement between data and the sum of signal and background predictions is essential to perform the unfolding.

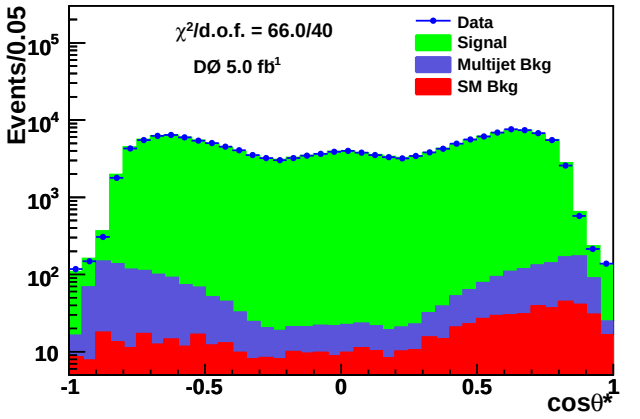

FIG. 5: [color online] Comparisons of the $\cos\theta^*$ between data and the sum of signal and background predictions for combined CC and CE events.

DETECTOR RESOLUTION AND ACCEPTANCE

The finite energy resolution in the determination of the track curvature may result in the assignment of events in different bins of invariant mass and in changes in the forward/backward classifications. These bin migration effects in the raw A_{FB} distribution are corrected using an unfolding procedure based on the iterative application of the matrix inversion method [34], as in a previous D0 analysis [25]. The CC and CE raw A_{FB} distributions are unfolded separately and then combined. We correct for both the wrong classification in terms of dielectron invariant mass and for the wrong forward/backward assignment by defining four detector response matrices. The response matrix R_{ij}^{FF} represents the probability that an event which at the generator level was classified to correspond to forward scattering angles and to have M_{ee} in the j-th bin, to be reconstructed in the i-th bin in M_{ee}, without any change to the forward/backward assignment. We similarly define R_{ij}^{BB} matrix for events which are classified as backward both at the generator and at the reconstruction level, and the R_{ij}^{FB} and R_{ij}^{BF} matrices for events in which the forward/backward assignment changes due to detector and reconstruction effects. Tests of the unfolding procedure are performed comparing the generator level distribution with the one obtained after unfolding the events processed through the full detector simulation and reconstructed as data.

The bin purity is defined as the ratio between the number of events generated in a mass bin and also reconstructed in the same mass bin ($N_{gen}^{\rm reco}$) and the number of events reconstructed in this mass bin ($N^{\rm reco}$). The lowest purity occurs for the two mass bins below the Z pole ($81 < M_{ee} < 86.5$ GeV and $86.5 < M_{ee} < 89.5$ GeV) and is about 25%. Since the corrected MC can describe the data mass spectra with finer binning as shown in Fig. 4, these low purity bins can be well modeled. The rest of the mass bins have purity varying between 50% and 96%.

After unfolding for detector resolution effects, the data are further corrected for acceptance. Using the corrected signal MC, we derive corrections for kinematic and geometric acceptance and for electron identification efficiencies.

CHARGE MISIDENTIFICATION RATE

The electron charge determines if an event is forward or backward. Mismeasurement of the sign may result in a dilution of A_{FB}. The charge misidentification probability f_q is given by

$$f_q = \frac{1}{2} N_{SS}/(N_{SS} + N_{OS}), \qquad (7)$$

where N_{SS} (N_{OS}) is the total number of $Z/\gamma^* \to e^+e^-$ events reconstructed with same-sign (opposite-sign) electrons. Since few same-sign events are observed in data, the corrected Z/γ^* MC is used to determine the shape of the misidentification probability as a function of dielectron invariant mass. The overall normalization is set by the misidentification probability determined from data around the Z pole. The misidentification probability is a function of M_{ee} and rises from 0.75% at $M_{ee} = 50$ GeV to 3.2% for $M_{ee} > 500$ GeV. The charge misidentification probability is included as a dilution factor $\mathcal{D}$ in A_{FB}, with $\mathcal{D} = (1 - 2f_q)/(1 - 2f_q + f_q^2)$ for CC events and $\mathcal{D} = (1 - 2f_q)$ for CE events.

SYSTEMATIC UNCERTAINTIES

The systematic uncertainties in the measurement of $\sin^2\theta^\ell_{\rm eff}$, and of the unfolded distribution of A_{FB}, g_V, and g_A, are listed below.

- **PDF**
  Uncertainties in the input parton distributions lead to uncertainties in the event acceptance. The systematic uncertainty due to the PDFs uncertainty is estimated by reweighting the central PDFs using the 40 CTEQ6.1M error sets, and the 90% C.L. uncertainty is calculated using the prescription suggested by the CTEQ group [5].

- **Electron energy scale and resolution**
  The energy scale and resolution for electrons in MC are corrected to match the observed Z boson pole position and width. The statistical uncertainties of the calibration parameters applied to MC are considered as a source systematic uncertainties. We vary each parameter by ±1 standard deviation to estimate the uncertainty on the final measured quantities.

- **MC statistics**
  To determine the systematic uncertainty due to the limited number of MC events, we divide the MC samples into ten independent sub-samples and perform ten pseudo-experiments. The spread of the unfolded A_{FB} and measured $\sin^2\theta^\ell_{\rm eff}$ from these pseudo-measurements divided by $\sqrt{10}$ is assigned as the systematic uncertainty due to the limited MC statistics.

- **Electron identification efficiency**
  To ensure the MC correctly models the electron and event selection efficiencies observed in data, we apply data/MC efficiency scale factors to the MC for forward and backward events separately. The bin-by-bin statistical fluctuations of these correction factors as a function of M_{ee} are taken into account and are propagated to the systematic uncertainties.

- **Background modeling**
  To estimate the uncertainty due to the multijet background, we vary the reversed electron shower shape requirements to obtain different mass spectra of multijet control samples. The uncertainties on SM backgrounds estimated using the MC mainly come from the uncertainties of the energy smearing, data and MC efficiency scale factors, and the uncertainty of the inclusive cross section for each process. For the $W+X$ inclusive background, additional uncertainties due to the modeling of the electron misidentification probability contributed by extra jets and the modeling of the W boson p_T (obtained from a comparison of PYTHIA and ALPGEN [35]) are also taken into account.

- **Charge misidentification**
  The statistical fluctuations in the misidentification probability measured from data in each mass bin are included as a systematic uncertainty.

The systematic uncertainties on the $\sin^2\theta^\ell_{\rm eff}$ extraction are summarized in Table IV. The primary systematic uncertainties are due to the PDFs (0.0005) and the EM energy calibration and resolution (0.0003). A correction factor is introduced to account for higher order electroweak corrections which are not included in PYTHIA. It is determined by generating ZGRAD2 and PYTHIA samples and comparing the A_{FB} distributions at the generator level. We find that there is a constant $+0.0005$ positive shift in the full $\sin^2\theta^\ell_{\rm eff}$ prediction from ZGRAD2 relative to the LO prediction from PYTHIA. We add this correction factor to the extracted value of $\sin^2\theta^\ell_{\rm eff}$.

The systematic uncertainties in the unfolded A_{FB} distribution are listed in Table V. In addition to the common sources listed above, uncertainties from higher order corrections and different SM inputs are taken into consideration. Higher order QCD, QED, and electroweak corrections can change the A_{FB} predictions and thus induce additional uncertainty. We compare PYTHIA A_{FB} distributions to those of ZGRAD2 [16] with the Z/γ^* boson p_T tuned to the RESBOS [17] prediction. RESBOS has the advantage of including most of the electroweak effects with a full simulation of the non-perturbative and next-to-leading-logarithm (NLL) QCD effects. The difference between the two predictions is taken as a systematic uncertainty. Different input values of $\sin^2\theta^\ell_{\rm eff}$ in PYTHIA will change the kinematic and geometric acceptances, and thus introduce uncertainty into the unfolding assumptions. We take $\sin^2\theta^\ell_{\rm eff}=0.232$ as the default input value, and vary it by the measured $\sin^2\theta^\ell_{\rm eff}$ uncertainty (0.001). We then repeat the unfolding procedure and take the largest deviation from the unfolded A_{FB} as the uncertainty.

The g^q_V and g^q_A couplings are extracted from the unfolded A_{FB} distribution and thus include all of the uncertainties (statistical and systematic) that affect the A_{FB} measurement. Additional uncertainties on the couplings from predictions with different PDF sets will be discussed later.

MEASUREMENT OF $\sin^2\theta^\ell_{\rm eff}$

The value of $\sin^2\theta^\ell_{\rm eff}$ is extracted from data by comparing the background-subtracted raw A_{FB} distribution with simulated A_{FB} templates corresponding to different input values of $\sin^2\theta^\ell_{\rm eff}$. This procedure avoids the

TABLE IV: Uncertainties for the $\sin^2\theta^\ell_{\rm eff}$ measurement. All uncertainties are symmetric.

Uncertainty source	$\Delta \sin^2\theta^\ell_{\rm eff}$
Statistical	0.00080
Systematics	0.00061
PDF/Acceptance	0.00048
EM scale/resolution	0.00029
MC Statistics	0.00020
Electron identification	0.00008
Bkg. modeling	0.00008
Charge misidentification	0.00004
Higher order	0.00008
Total uncertainty	0.00102

TABLE V: Systematic uncertainties per bin for the unfolded A_{FB} measurement. All uncertainties are symmetric.

M_{ee} (GeV)	EM scale/ resolution	Electron identification	Bkg. modeling	MC Statistics	PDF/ Acceptance	Charge mis-identification	QCD, QED	Input $\sin^2\theta^\ell_{\rm eff}$	Total
$50-60$	0.009	0.001	0.002	0.011	0.015	0.002	0.008	0.002	0.023
$60-70$	0.002	0.004	0.001	0.014	0.005	0.002	0.012	0.001	0.019
$70-75$	0.003	0.003	0.001	0.015	0.003	0.002	0.012	< 0.001	0.020
$75-81$	0.002	0.001	< 0.001	0.008	< 0.001	0.001	0.010	0.001	0.013
$81-86.5$	0.002	< 0.001	< 0.001	0.005	0.008	< 0.001	0.005	0.001	0.011
$86.5-89.5$	0.001	< 0.001	< 0.001	0.003	0.002	< 0.001	0.002	0.001	0.004
$89.5-92$	0.001	< 0.001	< 0.001	0.002	0.002	< 0.001	0.002	0.001	0.003
$92-97$	0.001	< 0.001	< 0.001	0.002	0.002	< 0.001	0.004	0.001	0.005
$97-105$	0.002	< 0.001	< 0.001	0.005	0.007	0.001	0.008	0.001	0.012
$105-115$	0.002	0.001	< 0.001	0.008	0.002	0.002	0.011	0.001	0.014
$115-130$	0.003	0.002	0.003	0.010	0.004	0.004	0.011	< 0.001	0.017
$130-180$	0.001	0.005	0.002	0.006	0.014	0.011	0.013	0.001	0.024
$180-250$	0.002	0.002	0.002	0.003	0.010	0.011	0.006	< 0.001	0.017
$250-500$	0.001	0.001	0.002	0.008	0.001	0.019	0.004	< 0.001	0.022
$500-1000$	0.001	< 0.001	< 0.001	< 0.001	< 0.001	0.016	< 0.001	< 0.001	0.016

increase of the systematic uncertainty of the measurement introduced by the use of the unfolding procedure and maximizes the statistical significance of the final result. Although variations in $\sin^2\theta^\ell_{\rm eff}$ have some effect over the full mass range $50 < M_{ee} < 1000$ GeV, the central value is predominantly determined by the events in the Z pole region, where the statistics are highest and the effects of background are smallest. Using events in the range $70 < M_{ee} < 130$ GeV, we measure $\sin^2\theta^\ell_{\rm eff} = 0.2304 \pm 0.0008$ (stat.) ± 0.0006 (syst.) using PYTHIA. We then include higher order electroweak corrections using the ZGRAD2 program. Taking into account the effect of higher order corrections results in a central value of $\sin^2\theta^\ell_{\rm eff} = 0.2309 \pm 0.0008$ (stat.) ± 0.0006 (syst.). We also check the $\sin^2\theta^\ell_{\rm eff}$ predictions using ZGRAD2 and ZFITTER [36] using the same input SM parameters and find the two results are consistent. Higher order electroweak and QCD corrections included in ZFITTER and not implemented in ZGRAD2 have a negligible impact on the $\sin^2\theta^\ell_{\rm eff}$ measurement. Therefore, our measured $\sin^2\theta^\ell_{\rm eff}$ can be directly compared with the values measured by the LEP and SLD Collaborations [15]. The comparison is shown in Fig. 6. The most precise measurements are the LEP b-quark forward-backward asymmetry, $A^{0,b}_{FB}$, the SLD left-right asymmetry, A_{lr}(SLD), the LEP τ-lepton polarisation measurement, $A_l(P_\tau)$, and the SLD lepton asymmetry, $A^{0,\ell}_{FB}$. Our result is more precise than the LEP combined inclusive hadronic charge asymmetry measurement, and comparable in precision with the LEP c-quark forward-backward asymmetry $A^{0,c}_{FB}$.

MEASUREMENT OF THE UNFOLDED A_{FB} DISTRIBUTION

The final unfolded A_{FB} distribution using both CC and CE events is shown in Fig. 7 and Table VI, together with PYTHIA and ZGRAD2 predictions. Because of the migration between mass bins, the correlation matrix is important for events near the Z pole region. The correlation coefficients are shown in Table VII. In the mass bins 130–180 and 250–500 GeV small deviations (< 2 standard deviations) are observed. The χ^2/d.o.f between data and prediction is 15.3/15 for PYTHIA, and 12.8/15

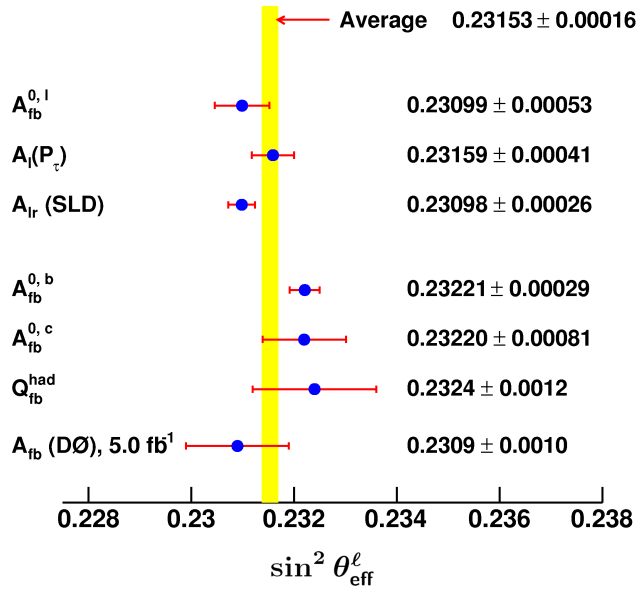

FIG. 6: Comparison of measured $\sin^2\theta_{\rm eff}^{\ell}$ with results from other experiments. The average is a combination of $A_{FB}^{0,\ell}$, $A_l(P_\tau)$, A_{lr}(SLD), $A_{FB}^{0,b}$, $A_{FB}^{0,c}$, and $Q_{FB}^{\rm had}$ measurements from the LEP and SLD Collaborations.

for ZGRAD2.

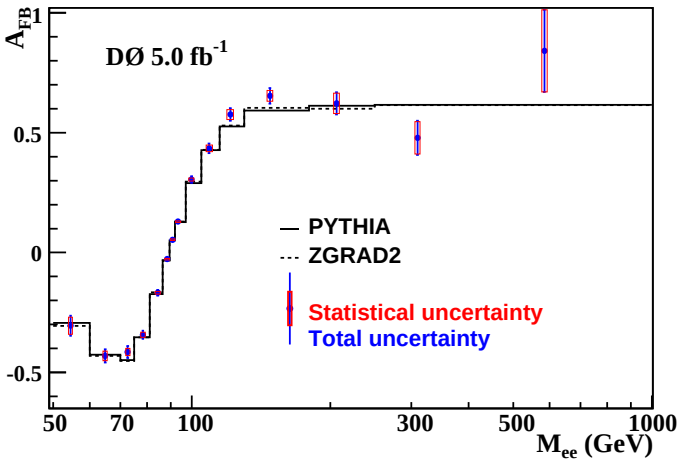

FIG. 7: Comparison between the unfolded A_{FB} (points) and the PYTHIA (solid curve) and ZGRAD2 (dashed line) predictions. The boxes and vertical lines show the statistical and total uncertainties, respectively.

MEASUREMENT OF $g_V^{u(d)}$ AND $g_A^{u(d)}$ FROM THE UNFOLDED DISTRIBUTION

We extract the individual quark couplings by comparing the unfolded A_{FB} distribution to templates generated with RESBOS for different values of the Z-light quark couplings. To determine $g_V^{u(d)}$ and $g_A^{u(d)}$, the couplings of electrons to Z bosons are fixed to their SM values and $\sin^2\theta_{\rm eff}^{\ell}$ is fixed to the global fit value 0.23153 [15]. A two-dimensional χ^2 fit [38] is used to constraint the couplings, and a four-dimensional fit is presented as reference. The two-dimensional fit is performed by fixing the u quark (d quark) couplings to their SM values when fitting d quark (u quark) couplings, while the four-dimensional fit is performed by letting the u quark and d quark couplings vary simultaneously. The best fit values, together with results from other experiments, are shown in Table VIII. Figure 8 depicts the 68% C.L. contours of the χ^2 fit and the contours of the theoretical uncertainty from the PDF uncertainties determined using the CTEQ prescription [5]. The correlation coefficients between g_V^u, g_A^u, g_V^d, and g_A^d are shown in Table IX, without the PDF uncertainty included. The comparisons between different measurements from LEP [15], H1 [37], CDF [21], and D0 are shown in Fig. 9. Because of the high statistics of our data sample, and the reduced ambiguity in the quark content of the initial state, these are the world's most precise direct measurements of g_V^u, g_A^u, g_V^d, and g_A^d to date.

CONCLUSIONS

We have measured the forward-backward charge asymmetry in $p\bar{p} \rightarrow Z/\gamma^* \rightarrow e^+e^-$ events and extracted $\sin^2\theta_{\rm eff}^{\ell}$, $g_V^{u(d)}$ and $g_A^{u(d)}$ using 5.0 fb^{-1} of integrated luminosity collected by the D0 experiment at $\sqrt{s} = 1.96$ TeV. The measured forward-backward charge asymmetry in the range $50 < M_{ee} < 1000$ GeV agrees with the theoretical predictions. The measured $\sin^2\theta_{\rm eff}^{\ell}$ value can be directly compared with the LEP and SLD results, and the overall $\sin^2\theta_{\rm eff}^{\ell}$ uncertainty for light quarks obtained is smaller than the combined uncertainty in the LEP measurements of the inclusive hadronic charge asymmetry. We also present the most precise direct measurement to date of g_V^u, g_A^u, g_V^d, and g_A^d.

Although the uncertainty of our $\sin^2\theta_{\rm eff}^{\ell}$ measurement is still larger than that of the current world average, with about 10 fb^{-1} of integrated luminosity expected by the end of Tevatron Run II, a combined result of CDF and D0 A_{FB} measurements in both dielectron and dimuon

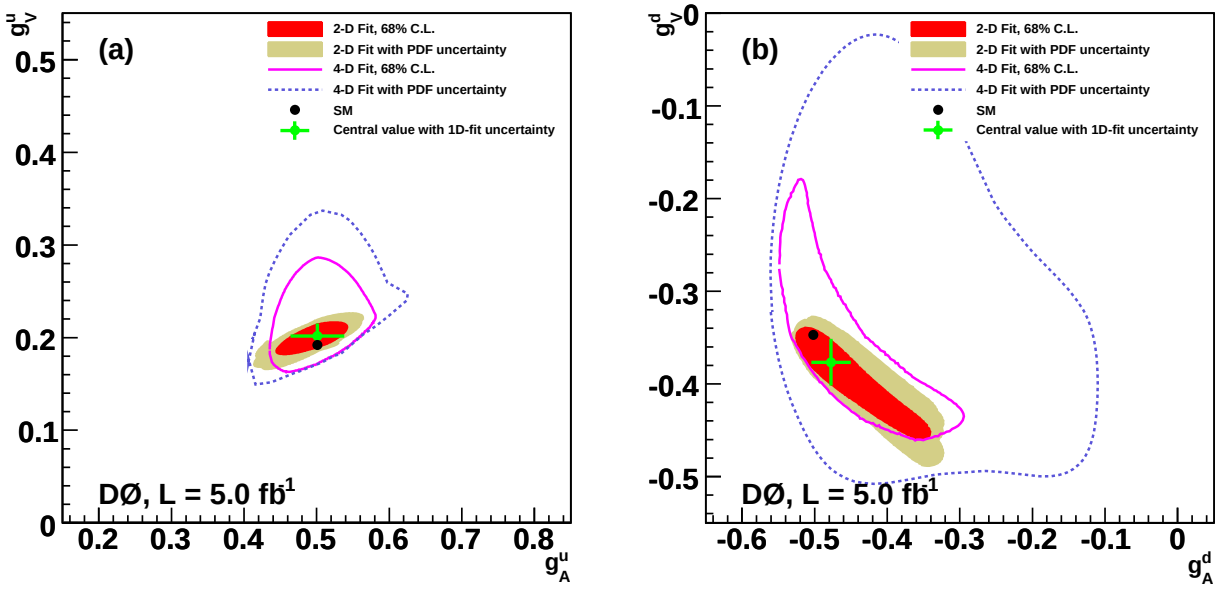

FIG. 8: [color online] The 68% C.L. contours of (a) g_V^u and g_A^u, and (b) g_V^d and g_A^d from a two-dimensional and a four-dimensional χ^2 fit with statistical and systematic uncertainties. The outer regions are determined by the theoretical PDF uncertainty. The two-dimensional correlation contours correspond to $\Delta\chi^2 = 2.3$ for different g_A and g_V parameters, as obtained from two-parameter (shaded regions) and four-parameter (solid and dashed curves) fits. The value 2.3 corresponds to the 68% C.L. region in two dimensions. In the case of four-parameter fit, the curve is a projection onto the two-dimensional plane of the envelope of the four-dimensional $\Delta\chi^2 = 4.72$ surface. The crosses indicate the best two-dimensional fit values, and the uncertainties correspond to the one-dimensional limits.

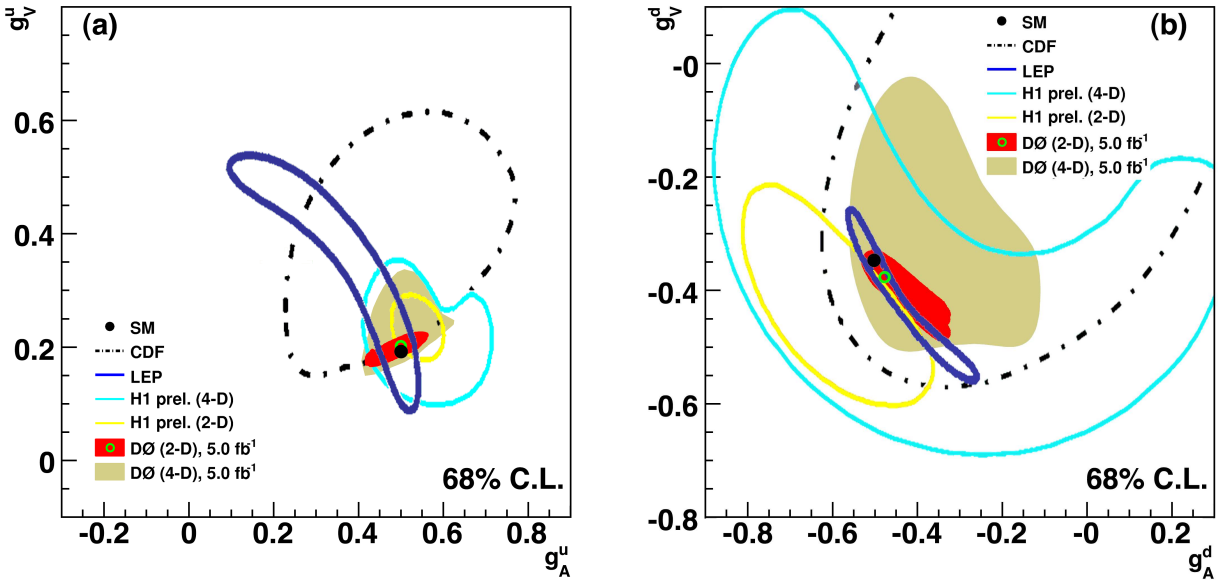

FIG. 9: [color online] The 68% C.L. contours of (a) g_V^u and g_A^u, and (b) g_V^d and g_A^d measured by D0 compared with other experiments. The LEP and CDF Collaborations performed fits with four free parameters to determine these couplings, while we and the H1 Collaboration performed both two and four free parameters fits. The LEP results have another solution (not shown) which is excluded by the H1, CDF and D0 results.

TABLE VI: The unfolded A_{FB} distribution compared with the theoretical predictions. The first column shows the mass ranges used. The second column shows the cross section weighted average of the invariant mass in each mass bin derived from PYTHIA. The third and fourth columns show the A_{FB} predictions from PYTHIA and ZGRAD2. The last column is the unfolded A_{FB}, where the first uncertainty is statistical and the second is systematic.

M_{ee} (GeV)	$\langle M_{ee} \rangle$ (GeV)	Predicted A_{FB}		Unfolded A_{FB}
		PYTHIA	ZGRAD2	
$50-60$	54.5	-0.293	-0.307	$-0.305 \pm 0.036 \pm 0.023$
$60-70$	64.9	-0.426	-0.431	$-0.431 \pm 0.020 \pm 0.019$
$70-75$	72.6	-0.449	-0.452	$-0.415 \pm 0.015 \pm 0.020$
$75-81$	78.3	-0.354	-0.354	$-0.343 \pm 0.011 \pm 0.013$
$81-86.5$	84.4	-0.174	-0.166	$-0.168 \pm 0.006 \pm 0.011$
$86.5-89.5$	88.4	-0.033	-0.031	$-0.028 \pm 0.003 \pm 0.004$
$89.5-92$	90.9	0.051	0.052	$0.054 \pm 0.003 \pm 0.003$
$92-97$	93.4	0.127	0.129	$0.129 \pm 0.003 \pm 0.005$
$97-105$	99.9	0.289	0.296	$0.305 \pm 0.007 \pm 0.012$
$105-115$	109.1	0.427	0.429	$0.435 \pm 0.014 \pm 0.014$
$115-130$	121.3	0.526	0.530	$0.576 \pm 0.021 \pm 0.017$
$130-180$	147.9	0.593	0.603	$0.654 \pm 0.022 \pm 0.024$
$180-250$	206.4	0.613	0.600	$0.623 \pm 0.043 \pm 0.017$
$250-500$	310.5	0.616	0.615	$0.479 \pm 0.068 \pm 0.022$
$500-1000$	584.4	0.616	0.615	$0.842 \pm 0.171 \pm 0.016$

TABLE VII: Correlation coefficients between different M_{ee} bins. Only half of the symmetric correlation matrix is presented.

Mass bin	1	2	3	4	5	6	7	8	9	10	11	12	13	14	15
1	1.00	0.24	0.03	0.00	0.00	0.00	0.00	0.00	0.00	0.00	0.00	0.00	0.00	0.00	0.00
2		1.00	0.39	0.06	0.02	0.02	0.02	0.01	0.00	0.00	0.00	0.00	0.00	0.00	0.00
3			1.00	0.46	0.11	0.04	0.03	0.02	0.00	0.00	0.00	0.00	0.00	0.00	0.00
4				1.00	0.51	0.15	0.07	0.04	0.01	0.00	0.00	0.00	0.00	0.00	0.00
5					1.00	0.72	0.32	0.11	0.01	0.00	0.00	0.00	0.00	0.00	0.00
6						1.00	0.78	0.40	0.03	0.00	0.00	0.00	0.00	0.00	0.00
7							1.00	0.80	0.13	0.01	0.00	0.00	0.00	0.00	0.00
8								1.00	0.48	0.04	0.00	0.00	0.00	0.00	0.00
9									1.00	0.38	0.03	0.00	0.00	0.00	0.00
10										1.00	0.28	0.01	0.00	0.00	0.00
11											1.00	0.16	0.00	0.00	0.00
12												1.00	0.06	0.00	0.00
13													1.00	0.06	0.00
14														1.00	0.02
15															1.00

channels has the potential to substantially impact the world average value of $\sin^2\theta^{\ell}_{\rm eff}$. In addition to a reduction of the dominant statistical uncertainties, many of the systematic uncertainties have a strong statistical component or will decrease with higher statistics, for example the electron energy scale and resolution. To match the precision of the current world average of $\sin^2\theta^{\ell}_{\rm eff}$, the theoretical uncertainty due to PDFs need to be reduced in similar proportions as the experimental uncertainties of the measurement.

ACKNOWLEDGEMENTS

We thank the staffs at Fermilab and collaborating institutions, and acknowledge support from the DOE and NSF (USA); CEA and CNRS/IN2P3 (France); FASI, Rosatom and RFBR (Russia); CNPq, FAPERJ, FAPESP and FUNDUNESP (Brazil); DAE and DST (India); Colciencias (Colombia); CONACyT (Mexico); KRF and KOSEF (Korea); CONICET and UBACyT (Argentina); FOM (The Netherlands); STFC and the Royal Society (United Kingdom); MSMT and GACR (Czech Republic); CRC Program and NSERC (Canada); BMBF and DFG (Germany); SFI (Ireland); The Swedish Research Council (Sweden); and CAS and CNSF (China).

TABLE VIII: Measured $g_V^{u(d)}$ and $g_A^{u(d)}$ values from different experiments compared with the SM predictions. The D0 results are derived from best two-dimensional and four-dimensional χ^2 fit, given with their total uncertainty.

	g_A^u	g_V^u	g_A^d	g_V^d
D0 (2-D)	0.501 ± 0.061	0.202 ± 0.025	-0.477 ± 0.112	-0.377 ± 0.081
D0 (4-D)	0.501 ± 0.110	0.201 ± 0.112	-0.497 ± 0.165	-0.351 ± 0.251
CDF [21](4-D)	$0.441^{+0.218}_{-0.186}$	$0.399^{+0.166}_{-0.199}$	$-0.016^{+0.358}_{-0.544}$	$-0.226^{+0.641}_{-0.304}$
H1 [22](4-D)	0.56 ± 0.10	0.05 ± 0.19	-0.77 ± 0.37	-0.50 ± 0.37
LEP [15](4-D)	$0.47^{+0.05}_{-0.33}$	$0.24^{+0.28}_{-0.11}$	$-0.52^{+0.05}_{-0.03}$	$-0.33^{+0.05}_{-0.07}$
SM [16]	0.501	0.192	-0.502	-0.347

TABLE IX: The correlation coefficients between g_V^u, g_A^u, g_V^d and g_A^d. Only half of the symmetric correlation matrix is presented.

	g_A^u	g_V^u	g_A^d	g_V^d
g_A^u	1.000			
g_V^u	0.470	1.000		
g_A^d	0.201	-0.606	1.000	
g_V^d	0.217	0.925	-0.813	1.000

[1] C. Amsler *et al.* (Particle Data Group), Phys. Lett. B **667**, 1 (2008) and 2009 partial update for the 2010 edition

[2] J. C. Collins and D. E. Soper, Phys. Rev. D **16**, 2219 (1977).

[3] R. Gelhaus, FERMILAB-THESIS-2005-22, UMI-31-91669 (2005).

[4] T. Sjöstrand *et al.*, Comput. Phys. Commun. **135**, 238 (2001). PYTHIA version v6.323 is used throughout.

[5] J. Pumplin *et al.*, J. High Energy Phys. **07**, 012 (2002); D. Stump *et al.*, J. High Energy Phys. **10**, 046 (2003).

[6] J. L. Rosner, Phys. Rev. D **54**, 1078 (1996); M. Carena, A. Daleo, B. A. Dobrescu, T. M. P. Tait, Phys. Rev. D **70**, 093009 (2004).

[7] H. Davoudiasl, J. L. Hewett, and T. G. Rizzo, Phys. Rev. Lett. **84**, 2080 (2000).

[8] A. Abulencia *et al.* (CDF Collaboration), Phys. Rev. Lett. **95**, 252001 (2005).

[9] D. Acosta *et al.* (CDF Collaboration), Phys. Rev. Lett. **95**, 131801 (2005).

[10] V. M. Abazov *et al.* (D0 Collaboration), Phys. Rev. Lett. **95**, 091801 (2005).

[11] V. M. Abazov *et al.* (D0 Collaboration), Phys. Rev. Lett. **95**, 161602 (2005).

[12] T. Aaltonen *et al.* (CDF Collaboration), Phys. Rev. Lett. **99**, 171802 (2007).

[13] V. M. Abazov *et al.* (D0 Collaboration), Phys. Rev Lett. **100**, 091802 (2008).

[14] A. Abulencia *et al.* (CDF Collaboration), Phys. Rev. Lett. **96**, 211801 (2006).

[15] G. Abbiendi *et al.* (LEP Collaborations ALEPH, DELPHI, L3 and OPAL; SLD Collaboration, LEP Electroweak Working Group, SLD Electroweak and Heavy Flavor Groups), Phys. Rep. **427**, 257 (2006).

[16] U. Baur, S. Keller, and W. K. Sakumoto, Phys. Rev. D **57**, 199 (1998); U. Baur, O. Brein, W. Hollik, C. Schappacher, D. Wackeroth, Phys. Rev. D **65**, 033007 (2002).

[17] C. Balazs and C. P. Yuan, Phys. Rev. D **56**, 5558 (1997).

[18] S. C. Bennett and C. E. Wieman, Phys. Rev. Lett. **82**, 2484 (1999).

[19] P. L. Anthony *et al.* (SLAC E158 Collaboration), Phys. Rev. Lett. **95**, 081601 (2005).

[20] G. P. Zeller *et al.* (NuTeV Collaboration), Phys. Rev. Lett. **88**, 091802 (2002) [Erratum-ibid. **90**, 239902 (2003)].

[21] D. Acosta *et al.* (CDF Collaboration), Phys. Rev. D **71**, 052002 (2005).

[22] A. Aktas *et al.* (H1 Collaboration), Phys. Lett. B **632**, 35 (2006).

[23] T. Affolder *et al.* (CDF Collaboration), Phys. Rev. Lett. **87**, 131802 (2001); F. Abe *et al.* (CDF Collaboration), Phys. Rev. Lett. **77**, 2616 (1996).

[24] B. Abbott *et al.* (D0 Collaboration), Phys. Rev. Lett. **82**, 4769 (1999).

[25] V. M. Abazov *et al.* (D0 Collaboration), Phys. Rev. Lett. **101**, 191801 (2008).

[26] T. Andeen *et al.*, FERMILAB-TM-2365 (2007).

[27] V. M. Abazov *et al.* (D0 Collaboration), Nucl. Instrum. Methods Phys. Res. Sect. A **565**, 463 (2006).

[28] D0 uses a cylindrical coordinate system with the z axis running along the beam axis in the proton direction. Angles θ and ϕ are the polar and azimuthal angles, respectively. Pseudorapidity is defined as $\eta = -\ln[\tan(\theta/2)]$ where θ is measured with respect to the interaction vertex. In the massless limit, η is equivalent to the rapidity $y = (1/2)\ln[(E+p_z)/(E-p_z)]$ and $\eta_{\rm det}$ is the pseudorapidity measured with respect to the center of the detector.

[29] R. Brun and F. Carminati, CERN Program Library Long Writeup W5013, 1993 (unpublished).

[30] P. B. Arnold, M. H. Reno, Nucl. Phys. **B 319**, 37 (1989) [Erratum-ibid. **B 330**, 284 (1990)].

[31] R. Hamberg, W. L. van Neerven, and T. Matsuura, Nucl. Phys. **B 359**, 343 (1991); [Erratum-ibid. **B 644**, 403 (2002)].

[32] J. M. Campbell and R. K. Ellis, Phys. Rev. D **60**, 113006

(1999).
[33] N. Kidonakis and R. Vogt, Phys. Rev. D **68**, 114014 (2003); M. Cacciari *et al.*, J. High Energy Phys. **04**, 68 (2004).
[34] G. L. Marchuk, Methods of Numerical Mathematics (Springer, Berlin, 1975).
[35] M. L. Mangano *et al.*, J. High Energy Phys. **07**, 001 (2003).
[36] D. Y. Bardin *et al.*, Z. Phys. C **44** 493 (1989); D. Y. Bardin *et al.*, Comput. Phys. Commun. **59**, 303 (1990).
[37] Z. Zhang, PoS DIS2010, 056 (2010).
[38] F. James, CERN Program Program Library Long Writeup D506, 1993 (unpublished)